

# La<sub>2</sub>O<sub>3</sub> Doped Graphitic Porous Carbon Derived from La(III) Ion Chelated Chitosan for High Performance Supercapacitor

Li Wang<sup>1</sup>, Xiaoxiao Du<sup>2</sup>, Yongjin Zou<sup>2,3</sup>, Cuili Xiang<sup>2,3,\*</sup>, Lei Jin<sup>4</sup>

<sup>1</sup> School of Applied Mathematics, Xiamen University of Technology, Xiamen, 361024, P.R. China

<sup>2</sup> Guangxi Key Laboratory of Information Materials, Guilin University of Electronic Technology, Guilin 541004, P.R. China

<sup>3</sup> Department of Physical and Environmental Sciences, University of Toronto Scarborough, Toronto, M1C 1A4, Canada

<sup>4</sup> School of Environmental Science and Engineering, Xiamen University of Technology, Xiamen, 361024, P.R. China

\*E-mail: [xiangcuili@guet.edu.cn](mailto:xiangcuili@guet.edu.cn)

Received: 3 May 2018 / Accepted: 21 June 2018 / Published: 5 August 2018

---

Biopolymers are excellent precursors to prepare porous carbon owing to their abundant resources, low cost, and unique properties. In this study, a La<sub>2</sub>O<sub>3</sub> doped graphitic porous carbon (La<sub>2</sub>O<sub>3</sub>/Chit-C) was prepared using La(III) ions chelated chitosan as starting materials. The prepared nanocomposite exhibited excellent electrochemical performance, which is suitable for the design of supercapacitor. It demonstrated a capacitance of 464.8 F g<sup>-1</sup> at a current density of 1 A g<sup>-1</sup>, which is higher than most of chitosan derived carbon materials. Furthermore, the nanocomposite showed good high-rate discharge capability and stability, demonstrating a potential application for electrochemical energy storage.

---

**Keywords:** Supercapacitor; Chitosan; La<sub>2</sub>O<sub>3</sub>; graphitic; Nanocomposite

## 1. INTRODUCTION

Portable devices are making our life better and easier, which are becoming independent of our life [1]. However, the electrical energy storage technology restrains their rapid development [2]. Therefore, it is still urgent to find a reliable energy storage device to power these portable devices. Supercapacitor is such a promising candidate with light weight, fast charge-discharge rate, and good cycling stability. Compared with traditional batteries, supercapacitor demonstrates higher power density, longer cycling life and lighter weight. Hence, it has been gained extensive interests in recent years [3-6].

The active materials of the electrode determine the most of the performance of supercapacitor. Therefore, to boost the capacitance of supercapacitor, design of new materials is the effective way [7, 8]. Porous carbon materials are the first preference for the physically charges accumulation in supercapacitor owing to their good stability, high surface area, excellent conductivity [9-11]. However, relatively low capacitance and energy density hinder their wide application. Metal oxides, conducting polymers are considered to be ideal materials for supercapacitor, which can store the charges through electrochemical reaction [12-14]. They can provide not only high capacitance, but also high energy density [15-17]. Nevertheless, poor conductivity and stability are still the unsolved problems. Combination of carbon nanomaterials with metal oxides to form hybrid materials is an alternative measure to solve these problems [18, 19]. However, facile doping metal oxide on carbon materials is still a challenge.

Chitosan is a nitrogen-rich organic biopolymer in nature [20, 21]. Nitrogen can be retained in the backbone of its carbonization product, which improves the wettability and conductivity of the porous carbon. However, direct carbonization of chitosan leads to low graphitic degree [20, 22, 23]. It has been well known that graphitic carbon shows better conductivity than disorder carbon. Therefore, production of graphitic carbon from chitosan is highly desired [24]. Chitosan can be used as an excellent adsorbent for the removal of heavy metals due to its amino groups and hydroxyl groups. It demonstrates strong capability for chelating with metal ions, which inspires us to fabricate metal oxides doped graphitic carbon by one-step carbonization. Therefore, in this study, the La(III) ions were chelated with chitosan and used as a precursor for pyrolysis. The prepared  $\text{La}_2\text{O}_3/\text{Chit-C}$  demonstrates excellent electrochemical performance, which is ideal for the fabrication of supercapacitor.

## 2. MATERIALS AND METHODS

### 2.1. Preparation of $\text{La}_2\text{O}_3/\text{Chit-C}$

Chitosan,  $\text{La}(\text{NO}_3)_3 \cdot 6\text{H}_2\text{O}$  and other chemicals are from commercial source and used as received. 1 g of chitosan powder was dissolved in 100 mL of acetic acid (1 wt%) solution gradually. Next, 0.1 g of  $\text{La}(\text{NO}_3)_3 \cdot 6\text{H}_2\text{O}$  was added to the mixture under stirring. Then the mixture was evaporated at 60 °C in a vacuum for 24 h. The soild was collected and placed in a tube furnace. The temperature of the furnace was kept at 800 °C for 3 h in a nitrogen flow. the furnace was then turned off and cooled down to room temperature natually. Finally, the sample was rinsed with deionized water thoroughly and dried at 80 °C for 12 h. The black powder was identified as  $\text{La}_2\text{O}_3/\text{Chit-C}$ . For comparison, the chitosan derived carbon was prepared under the identical condition and denoted as Chit-C.

### 2.2. Characterization of $\text{La}_2\text{O}_3/\text{Chit-C}$

The scanning electron microscopic (SEM) images were obtained from a Quanta 200 microscope. Transmission electron microscopic (TEM) images, high resolution TEM (HRTEM), selected-area electron diffraction (SAED) patterns, and energy dispersive X-ray (EDX) mapping were recorded on a JEOL 2100 electron microscope (Tecnai G2 F20 S-TWIN) at an accelerating voltage of

200 kV. The Fourier transform infrared (FTIR) spectra were recorded from an IR Nicolet 6700 spectrometer. The crystal structure of the samples was analyzed with a powder X-ray diffraction (XRD) (1820, Philips, The Netherlands) with Cu K $\alpha$  radiation ( $\lambda = 1.5418 \text{ \AA}$ ). The electronic states of the elements were examined with an X-ray photoelectron spectroscopy (XPS; ESCA 250). The surface area was studied by a Quantachrome Autosorb-iQ2 Automated gas sorption system at 77 K. The specific surface areas were calculated using the Brunauer–Emmett–Teller (BET) model.

### 2.3. Electrochemical tests

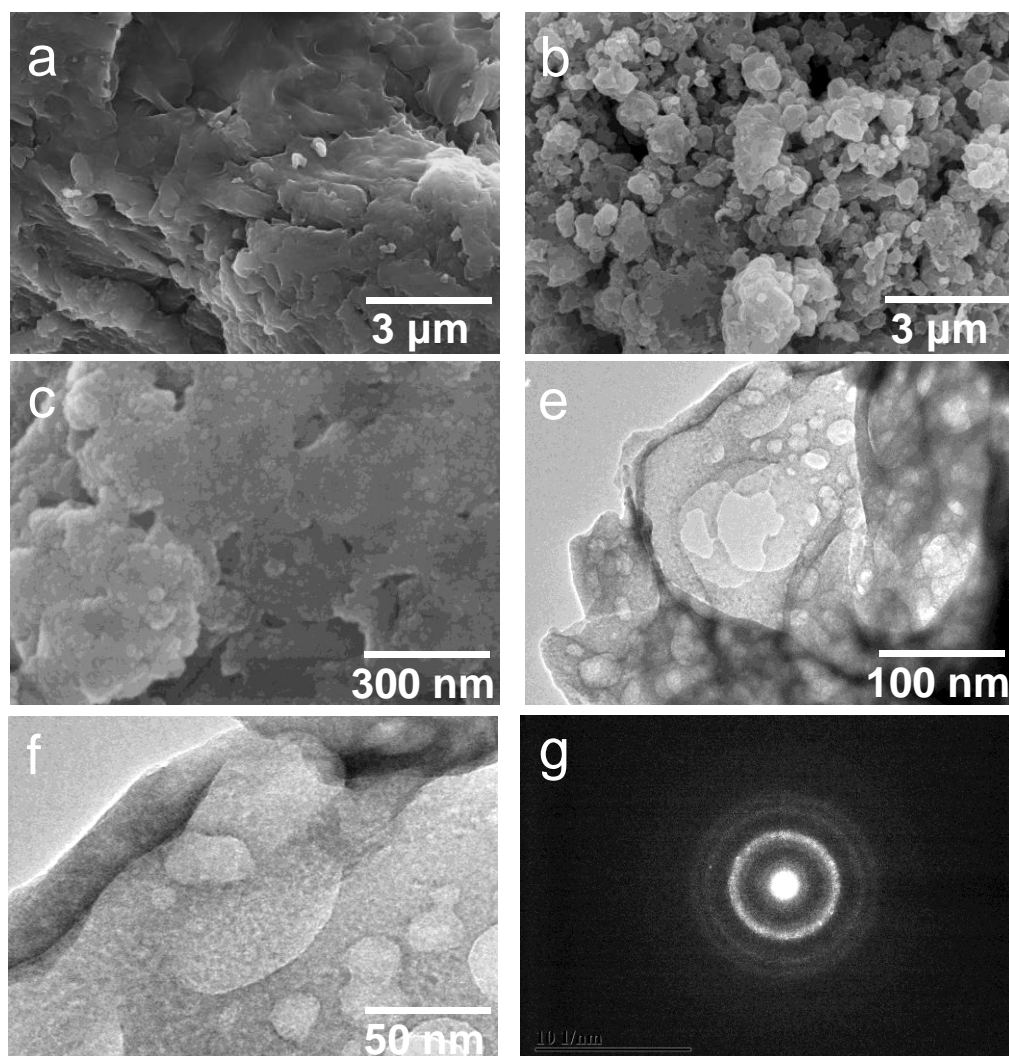
Electrochemical measurements including cyclic voltammetry (CV), galvanostatic charging/discharging (GCD) and electrochemical impedance spectroscopy (EIS) were performed using a CHI electrochemical station (760e, Shanghai) with a conventional three-electrode system in 6.0 M KOH. To prepare the working electrode, the as-synthesized samples (90 wt%) were mixed with 10 wt% of polyvinylidene fluoride and then ground it into slurry using alcohol as solvent. The slurry was then pressed onto nickel-foam ( $1 \times 1 \text{ cm}^2$ ) and dried at 80 °C for 2 h. The mass of the active material in working electrode was about 9 mg. A platinum foil electrode ( $0.5 \times 0.5 \text{ cm}^2$ ) and a saturated calomel electrode (SCE) and were used as the counter and reference electrodes, respectively. EIS measurements were conducted by applying an AC voltage with 10 mV amplitude in the frequency range of 0.01 Hz-100 kHz. The capacitance was calculated with established equation [24].

## 3. RESULTS AND DISCUSSION

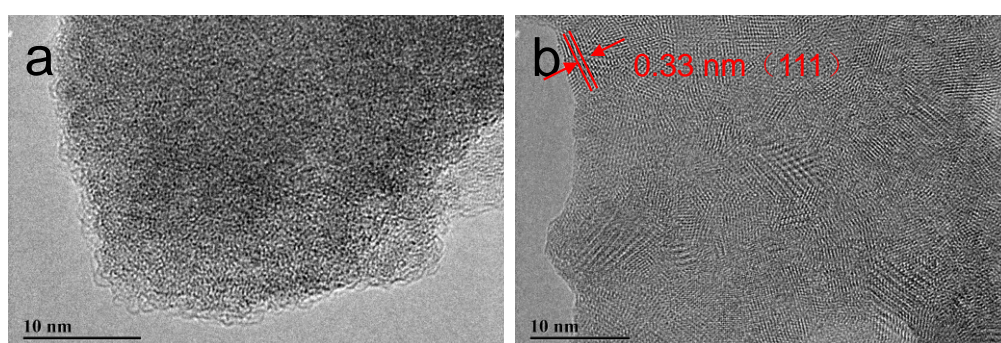
### 3.1 Characterization of La<sub>2</sub>O<sub>3</sub>/Chit-C

SEM and TEM were used to study the morphologies of La<sub>2</sub>O<sub>3</sub>/Chit-C and Chit-C. As shown in Figure 1a, the SEM image of Chi-C demonstrates irregular chunks, while La<sub>2</sub>O<sub>3</sub>/Chit-C shows porous structure (Figure 1b). It can be seen that the aggregated nanoparticles were doped on the carbon substrate (Figure 1c). The diameter of the nanoparticles is about 30 nm. TEM images further confirm that La<sub>2</sub>O<sub>3</sub>/Chit-C is in the form of porous texture (Figure 1e,f). Diffraction spots and rings observed from SAED pattern indicate the La<sub>2</sub>O<sub>3</sub>/Chit-C is typical in polycrystalline structure (Figure 1g) [25].

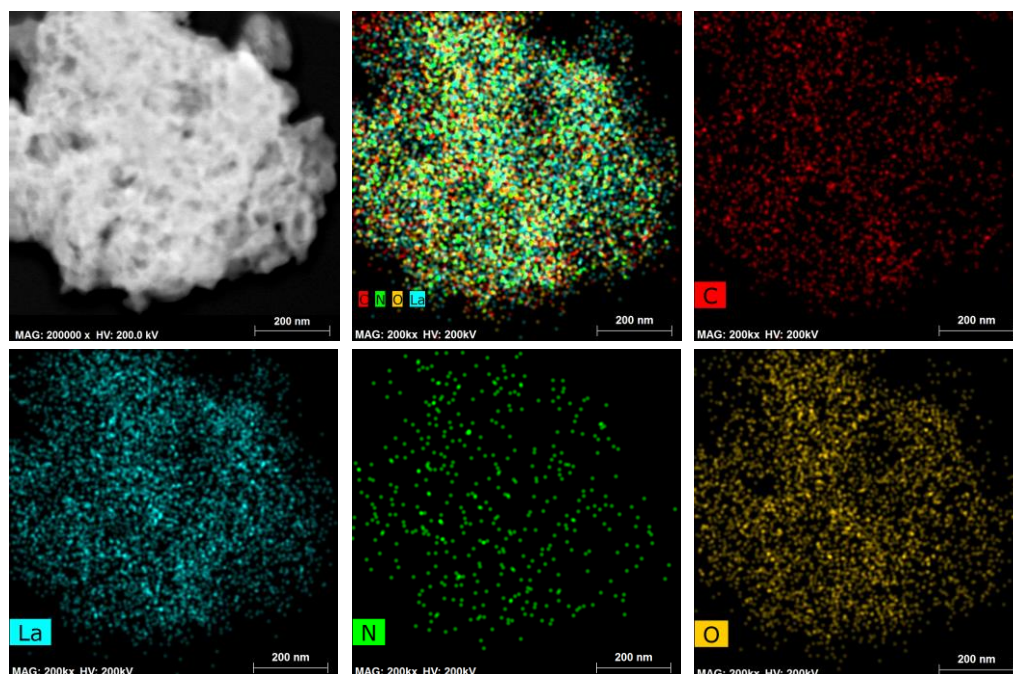
High resolution TEM was further conducted to examine the microstructure of the samples. As shown in Figure 2, only disordered carbon was observed in the sample of Chit-C (Figure 2a), while La<sub>2</sub>O<sub>3</sub>/Chit-C has a well-defined crystallized structure (Figure 2b). The lattice fringe is measured are 0.33 nm, which is close to graphite, suggesting a considerably high degree of graphitization. Graphitic carbon can be obtained using metal catalysts during the pyrolysis [26]. Presumably, La catalyzed the formation of graphitic carbon. Graphitic carbon possesses a higher conductivity than disordered carbon, which can demonstrate better electrochemical performance [27].



**Figure 1.** SEM images of (a) Chit-C and (b,c) La<sub>2</sub>O<sub>3</sub>/Chit-C; TEM images of (e,f) La<sub>2</sub>O<sub>3</sub>/Chit-C and (g) SEAD of La<sub>2</sub>O<sub>3</sub>/Chit-C.



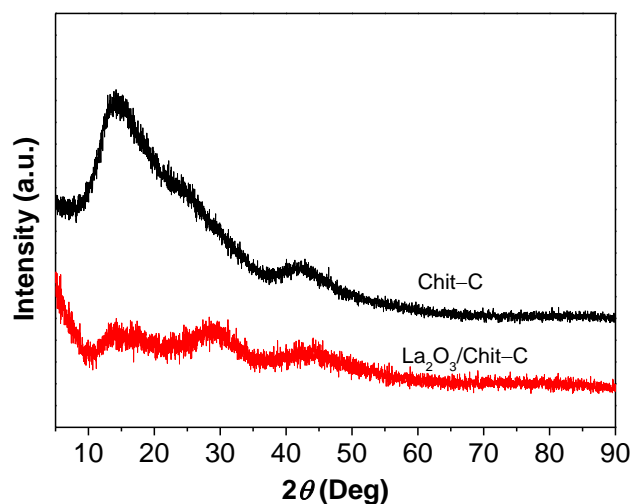
**Figure 2.** HRTEM images of (a) Chit-C and (b) La<sub>2</sub>O<sub>3</sub>/Chit-C.



**Figure 3.** EDX elemental mapping images of C, La, N, and O.

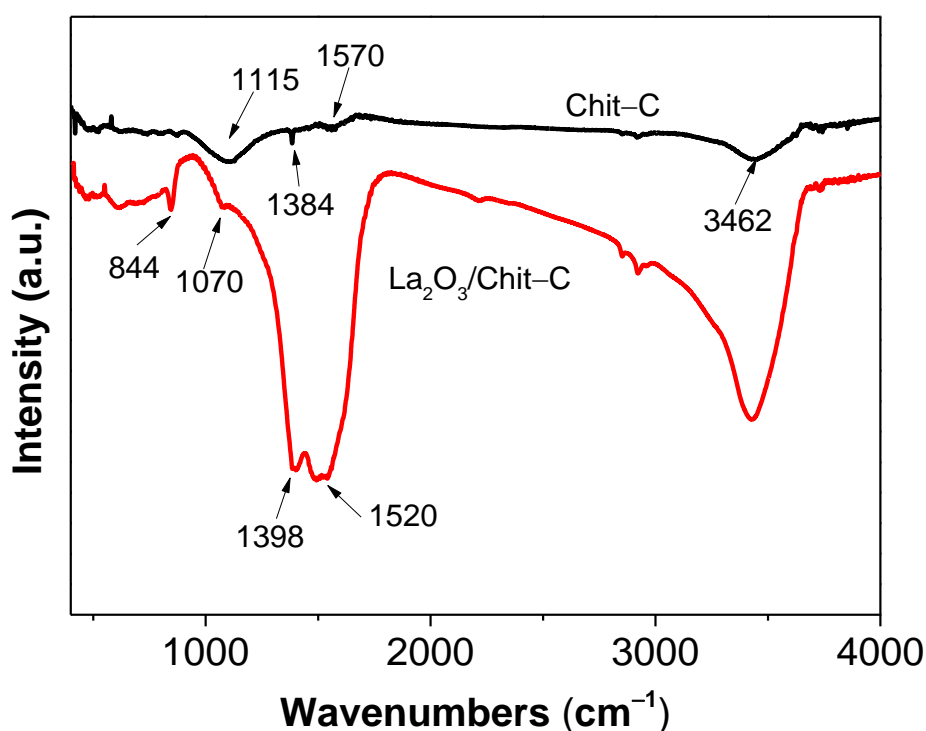
The EDX mapping results indicated that C, La, N, and O were well distributed in the whole  $\text{La}_2\text{O}_3/\text{Chit-C}$  nanocomposite. It consists of 53.6 at% C, 7.3 at% La, 35.5 at% O, and 3.56 at% N. The nanocomposite has a high content of oxygen, suggesting the La is in the form of oxide. N was found to be well doped in the nanocomposite, which is expected to improve the conductivity of the materials and contribute pseudocapacitance [22].

The XRD patterns of Chit-C and  $\text{La}_2\text{O}_3/\text{Chit-C}$  were shown in Figure.4. Two broad peaks centered at  $14.5^\circ$  and  $43.5^\circ$  can be found in the sample of Chit-C, which are indexed to the (002) and (101) planes of hexagonal carbon material, indicating the existence of amorphous carbon. In the sample of  $\text{La}_2\text{O}_3/\text{Chit-C}$ , two additional peaks located at  $14.4^\circ$  and  $29.1^\circ$ , which can be indexed to the (001) and (002) planes of  $\text{La}_2\text{O}_3$  (JCPDS 73-2141) [28], confirming La is in the form of  $\text{La}_2\text{O}_3$  in the composite.



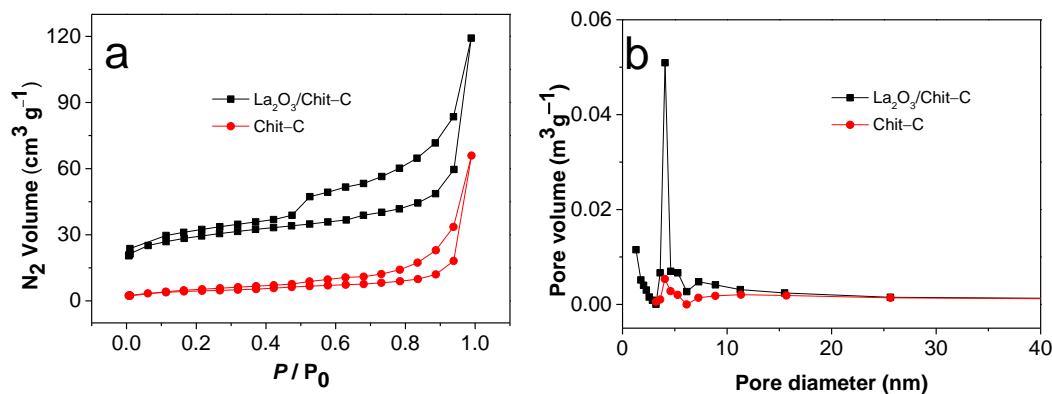
**Figure 4.** XRD patterns of the Chit-C and  $\text{La}_2\text{O}_3/\text{Chit-C}$ .

Figure 5 shows the FTIR spectra of Chit-C and  $\text{La}_2\text{O}_3/\text{Chit-C}$  composite. For the spectrum of Chit-C, the broad peak center at  $1115\text{ cm}^{-1}$  is assigned to the C–N stretching vibration. The peaks at  $1384$  and  $1570\text{ cm}^{-1}$  correspond to C=O and C=C stretching vibrations, respectively. The broad absorption band located at  $3462\text{ cm}^{-1}$  is attributed to N–H and O–H stretching vibrations [29]. Beside the peaks of Chit-C, The FTIR spectrum of  $\text{La}_2\text{O}_3/\text{Chit-C}$  shows several more peaks, which originated from  $\text{La}_2\text{O}_3$ . The peaks at  $1520\text{ cm}^{-1}$ ,  $1398\text{ cm}^{-1}$  and  $1070\text{ cm}^{-1}$  are attributed to the presence of carbonates, which is because the atmospheric  $\text{CO}_2$  and water can react on the surface of  $\text{La}_2\text{O}_3$  under ambient conditions and form the chemisorbed surface carbonates and bicarbonates [28]. The absorption bands at  $855\text{ cm}^{-1}$  can also be indexed to the carbonates in the initial formation mode, which is in agreement with previous report [28].



**Figure 5.** FTIR spectra of Chit-C and  $\text{La}_2\text{O}_3/\text{Chit-C}$ .

The surface areas of the Chit-C and  $\text{La}_2\text{O}_3/\text{Chit-C}$  samples were further investigated by  $\text{N}_2$  adsorption/desorption method. As shown in Figure 6a, the isotherm of  $\text{La}_2\text{O}_3/\text{Chit-C}$  demonstrates hysteresis loops at medium pressure ( $0.4\sim 0.9$ ), which indicates the existence of mesoporous pore. The BET surface areas are  $15.6$  and  $104\text{ m}^2\text{ g}^{-1}$  for the Chit-C and  $\text{La}_2\text{O}_3/\text{Chit-C}$  samples, respectively. The surface area of  $\text{La}_2\text{O}_3/\text{Chit-C}$  is about 6 times higher than Chit-C, indicating a more porous structure. The pore-size distribution curves for the Chit-C and  $\text{La}_2\text{O}_3/\text{Chit-C}$  present sharp peaks near  $4.8\text{ nm}$  (Figure 6b), which demonstrates that the doping of  $\text{La}_2\text{O}_3$  particles does not change the pore size in the composite.



**Figure 6.** (a) N<sub>2</sub> adsorption/desorption isotherms of the La<sub>2</sub>O<sub>3</sub>/Chit-C and Chit-C, and (b) pore-size distribution curves for the La<sub>2</sub>O<sub>3</sub>/Chit-C and Chit-C.

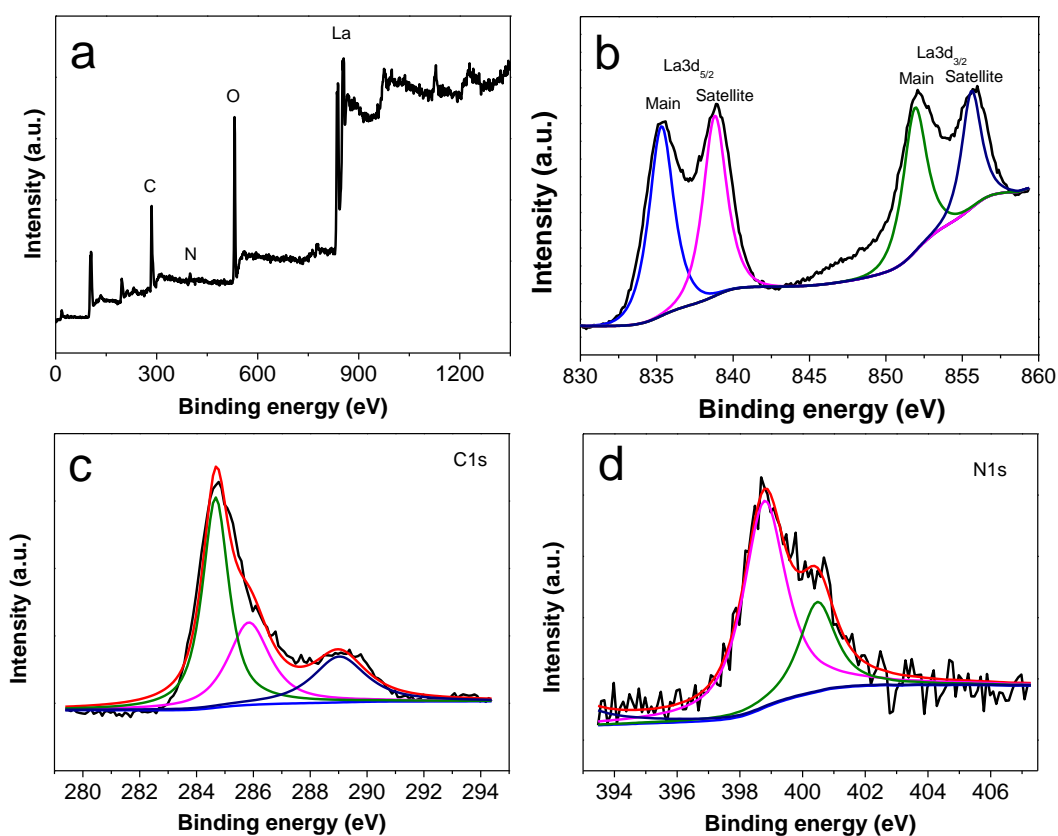


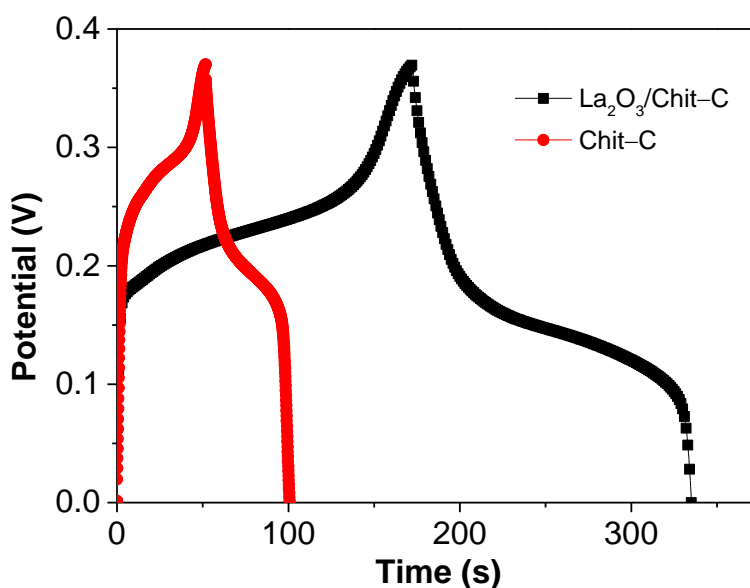
**Figure 7.** (a) Full XP spectrum of La<sub>2</sub>O<sub>3</sub>/Chit-C (a) and high-resolution spectra of the (b) La 3d, (c) C 1s, (d) N 1s.

The XPS spectra for La<sub>2</sub>O<sub>3</sub>/Chit-C were recorded and shown in Figure 7. The peaks of La 3d, C 1s, N 1s, and O 1s can be identified in the full spectrum of La<sub>2</sub>O<sub>3</sub>/Chit-C (Figure 7a). The high-resolution peaks were further fitted. The La 3d spectrum demonstrates two doublets and the energy peaks appearing on the high-energy side of the 3d<sub>5/2</sub> and 3d<sub>3/2</sub> peaks are the satellite peaks (Figure 7b). The energy difference between the 3d<sub>3/2</sub> and 3d<sub>5/2</sub> states is about 17 eV, which is identical with the value of La<sub>2</sub>O<sub>3</sub> [30]. The binding energy value of La 3d<sub>5/2</sub> is used for chemical state identification in La-containing oxides. The oxidation state is La<sup>3+</sup> if the binding energy of La 3d<sub>5/2</sub> is located in the range of 834.0-835.1 eV [31]. Therefore, it can be further concluded that La is in the form of La<sub>2</sub>O<sub>3</sub> in

the composite, which is in agreement of XRD results. The C 1s signal can be divided into three peaks corresponding to the C=C (284.7 eV), C–N/C–O (285.5 eV), and C=O (286.7 eV) bonds (Figure 7c), which are identical with reported results [24]. The signal of N 1s is deconvoluted into two main peaks related to different electronic states of the nitrogen functional groups: pyridinic N (398.6 eV) and pyrrolic N (400.9 eV) (Figure 7d), indicating a successful N-doping of the material [29]. For the pyridinic N and pyrrolic N, the N atoms are shown to be bonded with two  $sp^2$  carbon atoms and hence the lone-pairs may partake in the  $\pi$  system, a mechanism that is known to contribute Faradaic pseudocapacitance.

### 3.2 Electrochemical performance

Figure 8 shows the galvanostatic charge-discharge (GCD) curves of the Chit-C and  $La_2O_3/Chit-C$  electrodes at a current density of  $1 A g^{-1}$ . The curve of  $La_2O_3/Chit-C$  electrode shows typical feature of pseudocapacitor, which composes a rapid drop of potential and then a platform in the discharge process. The Chit-C electrode also shows similar curve, which is because of the pseudocapacitance originated from the nickel foam [32]. The specific capacitances were calculated to be 135.1 and  $464.8 F g^{-1}$ , respectively. The capacitance of  $La_2O_3/Chit-C$  electrode is more than 3 times higher than that of Chit-C, which indicates that the doping of  $La_2O_3$  significantly improve the electrochemical performance of Chit-C. As listed in Table 1, the capacitance of  $La_2O_3/Chit-C$  electrode is much higher than the reported chitosan derived carbon materials. The possible reasons are as follows: (1) La catalyzed the generation of graphitic carbon, which improves the conductivity of the porous carbon; (2) The role of N in the chitosan derived from chitosan not only improves the wettability of the materials, but also donates the pseudocapacitance; (3) The well-distributed  $La_2O_3$  nanoparticles on the porous carbon show good electrochemical activity.

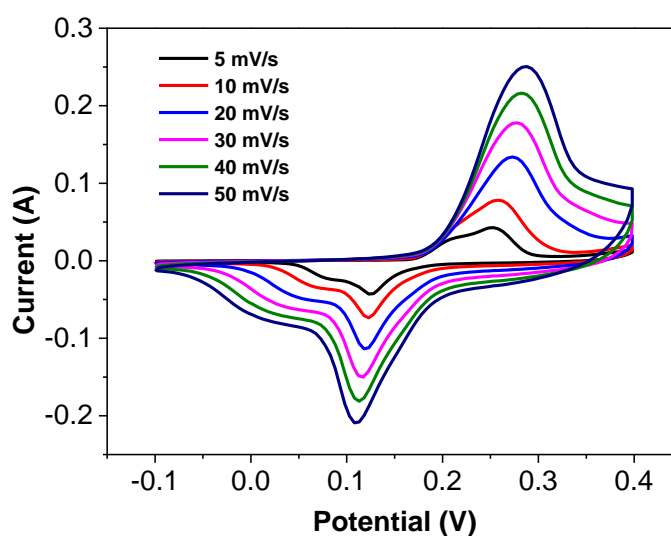


**Figure 8.** GCD curves of the Chit-C and  $La_2O_3/Chit-C$  electrodes at a current density of  $1 A g^{-1}$ .

**Table 1.** Specific capacitance of the La<sub>2</sub>O<sub>3</sub>/Chit-C electrode compared with literatures.

Sample	Current density (A g <sup>-1</sup> )	Specific capacitance (F g <sup>-1</sup> )	Reference
Chitosan-AC	1	264	[4]
GO-CS-copper	1	356	[21]
Carbon nanofiber aerogels	1	221	[33]
N-self-doped carbon framework	1	373	[34]
NC@CCS	1	173.1	[35]
PBE	0.5	250.5	[36]
NGA-900	0.2	244.4	[37]
GO-CS	1	320	[38]
NS-HPCS-750	1	272	[39]
Porous carbon foam	0.5	246.5	[40]
La <sub>2</sub> O <sub>3</sub> /Chit-C	1	464.8	This work

The CVs of La<sub>2</sub>O<sub>3</sub>/Chit-C at various scan rates are shown in Figure 9. It can be seen that a couple of redox peaks are located at around 0.2 V in the CV curves. When the scan rate is increased from 5 to 50 mV s<sup>-1</sup> in a 6.0 M KOH solution, the peak current densities increase with the scan rates. The shape of the CV curves well retained, indicating a rapid redox reaction of La<sub>2</sub>O<sub>3</sub>/Chit-C. The possible charge storage mechanism for La<sub>2</sub>O<sub>3</sub> can be expressed by the following equation[41]:

**Figure 9.** CV curves of the La<sub>2</sub>O<sub>3</sub>/Chit-C electrode at various scan rates in 6.0 M KOH solution.

The impedance characteristics of Chit-C and La<sub>2</sub>O<sub>3</sub>/Chit-C electrodes are shown in Figure 10. The Nyquist plots are composed of a small semicircle in the high-frequency region and a nearly vertical straight line in the low frequency region, indicating the samples possess the ideal capacitive

behaviors. The equivalent circuit diagram was used to fit the EIS data, which includes the solution resistance ( $R_s$ ), the charge transfer resistance ( $R_{ct}$ ), the pseudocapacitive element ( $C_L$ ) from redox process of  $\text{La}_2\text{O}_3$ , the Warburg diffusion element ( $W$ ), and the constant phase element ( $CPE$ ). The calculated charge-transfer resistance values for the Chit-C and  $\text{La}_2\text{O}_3/\text{Chit-C}$  electrodes were 0.8, and 0.5  $\Omega$ , respectively. The  $\text{La}_2\text{O}_3/\text{Chit-C}$  electrode had the lower charge-transfer resistance value than Chit-C, which is probably because the synergistic effect between the  $\text{La}_2\text{O}_3$  and Chit-C.

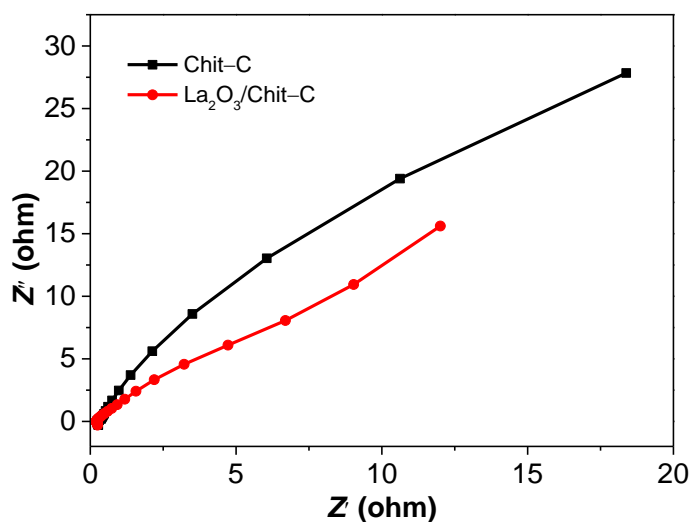


**Figure 10.** Nyquist plots of the as-synthesized materials.

The GCD curves at different current densities are shown in Figure 11. The shapes of the GCD curves were well kept even at high current density up to 10  $\text{A g}^{-1}$ , indicating a good reversibility and capacitive performance. The  $\text{La}_2\text{O}_3/\text{Chit-C}$  composite retains 48% of its initial specific capacitance value when the current density is increased from 1 to 10  $\text{A g}^{-1}$ , indicating an excellent high-rate capability.

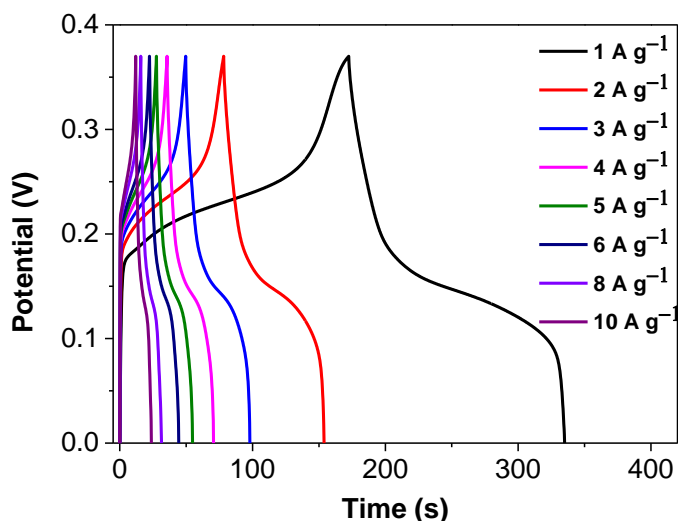


**Figure 11.** GCD curves of  $\text{La}_2\text{O}_3/\text{Chit-C}$  electrode at different densities.

The cycling stability of La<sub>2</sub>O<sub>3</sub>/Chit-C based supercapacitor was examined at the current density of 1 A g<sup>-1</sup>. As shown in Figure 12, the capacitance retained 90.6% of its initial capacitance, indicating the La<sub>2</sub>O<sub>3</sub>/Chit-C based supercapacitor has a good electrochemical stability.

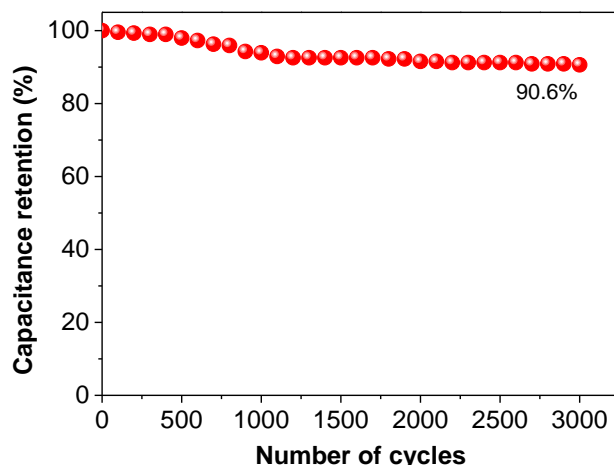


**Figure 12.** Cycling stability of the La<sub>2</sub>O<sub>3</sub>/Chit-C based supercapacitor

#### 4. CONCLUSIONS

La<sub>2</sub>O<sub>3</sub>/Chit-C nanocomposite was facilely synthesized by pyrolysis of La(III) ions chelated chitosan. La<sub>2</sub>O<sub>3</sub> nanoparticles were well distributed on the graphitic porous carbon. Compared with Chit-C, the La<sub>2</sub>O<sub>3</sub>/Chit-C nanocomposite shows much higher electrochemical performance, which could be attributed to the synergistic effect between the La<sub>2</sub>O<sub>3</sub> and porous carbon. The intimated contact between the La<sub>2</sub>O<sub>3</sub> and porous carbon not only improves the conductivity of the metal oxide, but also contributes the pseudocapacitance. The nanocomposite demonstrates a high capacitance of 464.8 F g<sup>-1</sup> at the current density of 1 A g<sup>-1</sup>. Furthermore, the supercapacitor shows excellent cycling stability, suggesting a promising application in energy storage.

#### ACKNOWLEDGEMENTS

The authors appreciate the funding support from NSFC (51561006, 51461011 and U1501242), the GXNSF (2016GXNSFFA380012, 2017GXNSFDA198018 and 2017AD23029), Natural Science Foundation Project of Fujian Province (2018J01527), and Fujian Science and Technology Guiding Project (Grant NO. 2018Y0079).

#### References

1. J. Chen, Z. Mao, L. Zhang, Y. Tang, D. Wang, L. Bie, B.D. Fahlman, *Carbon*, 130 (2018) 41-47.
2. L. Cao, M. Yang, D. Wu, F. Lyu, Z. Sun, X. Zhong, H. Pan, H. Liu, Z. Lu, *Chem. Commun.*, 53 (2017) 1615-1618.
3. Y. Cao, B. Lin, Y. Sun, H. Yang, X. Zhang, *Electrochim. Acta*, 174 (2015) 41-50.
4. M. Genovese, H. Wu, A. Virya, J. Li, P. Shen, K. Lian, *Electrochim. Acta*, 273 (2018) 392-401.
5. Y. Li, B. Guan, A. Maclennan, Y. Hu, D. Li, J. Zhao, Y. Wang, H. Zhang, *Electrochim. Acta*, 241

- (2017) 395-405.
6. Y. Liu, L. Liu, Y. Tan, L. Niu, L. Kong, L. Kang, F. Ran, *Electrochim. Acta*, 262 (2018) 66-73.
  7. A.A. Yadav, A.C. Lokhande, J.H. Kim, C.D. Lokhande, *J. Industrial Eng. Chem.*, 56 (2017) 90-98.
  8. M. Aghazadeh, M.R. Ganjali, P. Norouzi, *Mater. Res. Express*, 3 (2016) 055013.
  9. X. Zhao, S. Wang, Q. Wu, *Electrochim. Acta*, 247 (2017) 1140-1146.
  10. H. Xuan, G. Lin, F. Wang, J. Liu, X. Dong, F. Xi, *J. Solid State Electrochem.*, 21 (2017) 2241-2249.
  11. Y. Liu, B. Huang, X. Lin, Z. Xie, *J. Mater. Chem. A*, 5 (2017) 13009-13018.
  12. M. Liu, X. Wang, D. Zhu, L. Li, H. Duan, Z. Xu, Z. Wang, L. Gan, *Chem. Eng. J.*, 308 (2017) 240-247.
  13. L. Gao, J.U. Surjadi, K. Cao, H. Zhang, P. Li, S. Xu, C. Jiang, J. Song, D. Sun, Y. Lu, *ACS Appl. Mater. Interfaces*, 9 (2017) 5409-5418.
  14. Z. Yan, Q. Hu, G. Yan, H. Li, K. Shih, Z. Yang, X. Li, Z. Wang, J. Wang, *Chem. Eng. J.*, 321 (2017) 495-501.
  15. Z. Zhang, H. Zhang, X. Zhang, D. Yu, Y. Ji, Q. Sun, Y. Wang, X. Liu, *J. Mater. Chem. A*, 4 (2016) 18578-18584.
  16. G. Sun, H. Xie, J. Ran, L. Ma, X. Shen, J. Hu, H. Tong, *J. Mater. Chem. A*, 4 (2016) 16576-16587.
  17. X. Leng, Y. Shao, L. Wu, S. Wei, Z. Jiang, G. Wang, Q. Jiang, J. Lian, *J. Mater. Chem. A*, 4 (2016) 10304-10313.
  18. H.-Y. Wang, Y.-Y. Hsu, R. Chen, T.-S. Chan, H.M. Chen, B. Liu, *Adv. Energy Mater.*, 5 (2015) 1500091.
  19. L. Peng, Y. Feng, Y. Bai, H.-J. Qiu, Y. Wang, *J. Mater. Chem. A*, 3 (2015) 8825-8831.
  20. A. Śliwak, N. Díez, E. Miniach, G. Gryglewicz, *J. Appl. Electrochem.*, 46 (2016) 667-677.
  21. S. Selvam, B. Balamuralitharan, S. Jegatheeswaran, M.Y. Kim, S.N. Karthick, J. Anandha Raj, P. Boomi, M. Sundrarajan, K. Prabakar, H.-J. Kim, *J. Mater. Chem. A*, 5 (2017) 1380-1386.
  22. P. Hao, Z. Zhao, Y. Leng, J. Tian, Y. Sang, R.I. Boughton, C.P. Wong, H. Liu, B. Yang, *Nano Energy*, 15 (2015) 9-23.
  23. S. Liu, Z. Li, X.X. Wang, X. Liu, W. Ye, Y.Z. Long, H. Li, P. Guo, X.S. Zhao, *Int. J. Electrochem. Sci.*, 12 (2017) 11244-11255.
  24. Y. Zou, C. Cai, C. Xiang, P. Huang, H. Chu, Z. She, F. Xu, L. Sun, H.-B. Kraatz, *Electrochim. Acta*, 261 (2018) 537-547.
  25. Y. Xu, Y. Peng, X. Zheng, K.D. Dearn, H. Xu, X. Hu, *Energy*, 83 (2015) 80-88.
  26. A. Aijaz, J. Masa, C. Rosler, W. Xia, P. Weide, A.J. Botz, R.A. Fischer, W. Schuhmann, M. Muhler, *Angew. Chem. Int. Ed.*, 55 (2016) 4087-4091.
  27. J. Wang, F. Ciucci, *Small*, 13 (2017).
  28. B.P. Gangwar, V. Palakollu, A. Singh, S. Kanvah, S. Sharma, *RSC Adv*, 4 (2014) 55407-55416.
  29. C. Cai, Y. Zou, C. Xiang, H. Chu, S. Qiu, Q. Sui, F. Xu, L. Sun, A. Shah, *Appl. Surf. Sci.*, 440 (2018) 47-54.
  30. F.J. Jing, N. Huang, Y.W. Liu, W. Zhang, X.B. Zhao, R.K. Fu, J.B. Wang, Z.Y. Shao, J.Y. Chen, Y.X. Leng, X.Y. Liu, P.K. Chu, *J. Biomed. Mater. Res. Part A*, 87 (2008) 1027-1033.
  31. A.A. Yadav, A.C. Lokhande, J.H. Kim, C.D. Lokhande, *Int. J. Hydrogen Energy*, 41 (2016) 18311-18319.
  32. M. Yu, W. Wang, C. Li, T. Zhai, X. Lu, Y. Tong, *NPG Asia Mater.*, 6 (2014) e129-e129.
  33. B. Ding, S. Huang, K. Pang, Y. Duan, J. Zhang, *ACS Sustain. Chem. Eng.*, 6 (2017) 177-185.
  34. Y. Hu, X. Tong, H. Zhuo, L. Zhong, X. Peng, *ACS Sustain. Chem. Eng.*, 5 (2017) 8663-8674.
  35. Z. Li, L. Yang, H. Cao, Y. Chang, K. Tang, Z. Cao, J. Chang, Y. Cao, W. Wang, M. Gao, C. Liu, D. Liu, H. Zhao, Y. Zhang, M. Li, *Carbohydrate Poly.*, 175 (2017) 223-230.
  36. X. Liu, X. Liu, B. Sun, H. Zhou, A. Fu, Y. Wang, Y.G. Guo, P. Guo, H. Li, *Carbon*, 130 (2018) 680-691.
  37. Y. Zhang, J.Y. Zhu, H.B. Ren, Y.T. Bi, L. Zhang, *Chin. Chem. Lett.*, 28 (2017) 935-942.
  38. G. Sun, B. Li, J. Ran, X. Shen, H. Tong, *Electrochim. Acta*, 171 (2015) 13-22.

39. S. Huo, M. Liu, L. Wu, M. Liu, M. Xu, W. Ni, Y.-M. Yan, *J. Power Sources*, 387 (2018) 81-90.
40. F. Zhang, T. Liu, G. Hou, T. Kou, L. Yue, R. Guan, Y. Li, *Nano Res.*, 9 (2016) 2875-2888.
41. A.A. Yadav, V.S. Kumbhar, S.J. Patil, N.R. Chodankar, C.D. Lokhande, *Ceram. Int.*, 42 (2016) 2079-2084.

© 2018 The Authors. Published by ESG ([www.electrochemsci.org](http://www.electrochemsci.org)). This article is an open access article distributed under the terms and conditions of the Creative Commons Attribution license (<http://creativecommons.org/licenses/by/4.0/>).